

Sculpting an AGB Mass-Loss Envelope into a Bipolar Planetary Nebula: High-Velocity Outflows in V Hydrae

Raghvendra Sahai¹, Ben E.K. Sugerman², Kenneth Hinkle³

raghvendra.sahai@jpl.nasa.gov

Received _____; accepted _____

High Velocity Outflows in V Hydrae

¹Jet Propulsion Laboratory, California Institute of Technology, 4800 Oak Grove Dr., Pasadena, CA 91109

²Goucher College, 1021 Dulaney Valley Rd Baltimore, MD 21204

³National Optical Astronomy Observatory, PO Box 26732, Tucson, AZ 85726

ABSTRACT

We have carried out high-resolution spectroscopic observations of the carbon star V Hya, covering the $4.6\mu\text{m}$ band of CO. These data, taken over 7 epochs, show that the circumstellar environment of V Hya consists of a complex high-velocity (HV) outflow containing at least six kinematic components with expansion velocities ranging between 70 and 120 km s^{-1} , together with a slow-moving normal outflow at about 10 km s^{-1} . Physical changes occur in the HV outflow regions on a time-scale as short as two days, limiting their extent to be $\lesssim 10^{16}$ cm. The intrinsic line-width for each HV component is quite large ($6 - 8\text{ km s}^{-1}$) compared to the typical values ($\sim 1\text{ km s}^{-1}$) appropriate for normal AGB circumstellar envelopes (CSEs), due to excess turbulence and/or large velocity gradients resulting from the energetic interaction of the HV outflow with the V Hya CSE. We have modelled the absorption features to set constraints on the temperature distribution in, and the mass ejection-rates for gas in the main HV components.

Subject headings: stars: AGB and post-AGB, stars: mass-loss, stars: carbon, ISM: jets and outflows, stars: individual (V Hydrae)

1. Introduction

Stars of mass about $(1 - 8) M_{\odot}$ live uneventful lives on the main sequence. But as AGB stars, they eject, over a period of 10^4 - 10^5 years or less, half or more of their mass in slow spherical winds. And then, in a very poorly understood short (few 100–1000 yr) phase, they are transformed first into aspherical pre-planetary nebulae (PPNs), which then evolve into aspherical planetary nebulae (PNs). Recent morphological studies with the Hubble Space Telescope (*HST*) support the idea that high-speed, jet-like outflows play a crucial role in

this transformation (Sahai & Trauger 1998, Sahai et al. 2007, Balick & Frank 2002). These outflows may be driven by an accretion disk around a binary companion (Morris 1987). However, evidence for such outflows is indirect; this phase is so short that few nearby stars are likely to be caught in the act.

One such star is carbon-rich V Hydrae (V Hya), well known for its collimated, high-velocity ($\gtrsim 50 \text{ km s}^{-1}$) outflows. The unusual nature of the mass ejections in V Hya was first noticed in single-dish observations of the CO J=1-0 line: e.g., (Kahane et al. 1988) concluded that the V Hya circumstellar envelope (CSE) consists of a primary outflow which is roughly isotropic, and expanding slowly (emitting over a velocity range of about 16 km s^{-1}), as well as a secondary bipolar outflow, which is expanding roughly twice as fast. Very high-velocity outflows were first seen via observations of individual P and R-branch lines in the fundamental vibration-rotation band of $^{12}\text{C}^{16}\text{O}$ (hereafter CO) at $4.6 \mu\text{m}$. These data, taken over two epochs by Sahai & Wannier (1988, hereafter SW88) showed the presence of several absorption components due to high-velocity (hereafter HV) gas up to $V_{exp} \approx 120 \text{ km s}^{-1}$. The absorption lines showed significant differences between the two epochs, implying changes in the physical properties of the HV outflow over year-long time-scales. This study provided the first direct evidence of the simultaneous presence of a slowly expanding envelope and such a high-velocity stellar wind in a mass-losing AGB carbon star. Evans (1991) found outflow velocities up to 155 km s^{-1} from optical spectroscopy, while Luttermoser & Brown (1992) found 3.6 cm continuum emission suggesting the presence of shock-heated gas in the HV outflow. High signal-to-noise millimeter-wave CO J=2–1 and 3–2 line profiles showed wide wings, indicating the presence outflowing gas at velocities of $\gtrsim 200 \text{ km s}^{-1}$ (Knapp et al. 1997: KJY97). Interferometric mapping of the CO J=2–1 & 3–2 emission resolved the high-velocity emission and showed that it came from an extended, bipolar and highly collimated outflow (Hirano et al. 2004: Hetal04). The optical spectrum of V Hya shows anomalously broad photospheric lines,

which Barnbaum, Morris & Kahane (1995) interpret in terms of rotation due to spin-up by a companion in a common envelope configuration, although alternative explanations have been presented (Luttermoser & Brown 1992, KJY97).

Sahai et al. (2003a; Setal03) used the Space Telescope Imaging Spectrograph onboard the *HST* to image highly excited HV material: they found a blob of hot, shocked gas (emitting in the [SII] λ 4069.7Å line) moving away from the central star with a projected radial velocity of -240 km s^{-1} relative to the systemic velocity. Setal03 also found a compact ($\approx 0.5''$), hot, slowly-expanding ($10\text{--}15 \text{ km s}^{-1}$) central disk-like structure, as well as a large ($\approx 20''$), cool, equatorially-flattened structure. Although the expansive kinematics of the former implies that it is not an accretion disk, Setal03 speculate that it may result from a recent phase of equatorially enhanced mass-loss, which may be enhancing the accretion process. In a successful search for binary companions of cool AGB stars via the far-UV emission from the former, Sahai et al. (2008) find that V Hya stands out amongst their survey objects as having the largest FUV flux, as well as the highest FUV-to-NUV flux ratio. They conclude that the FUV emission, which is many orders of magnitude larger than the contribution from the carbon star, is either directly or indirectly due to a companion star – photospheric emission from the companion in the first case, or an accretion disk around the companion, in the second case.

V Hya is thus the best example to date of an AGB star with an active, collimated outflow, dense equatorially-flattened structures possibly related to a central accretion disk, and an inferred binary companion.

In this paper, we report high-resolution, high signal-to-noise spectroscopy of the $4.6 \mu\text{m}$ band of CO and its isotopomers in V Hya, taken over 7 epochs spanning 2 years, in order to characterize and constrain the kinematic structure and time-variations of the HV outflow, and its hydrodynamic interaction with the normal envelope. Observations and data

reduction are described in §2, and the observational results are presented in §3. We interpret the spectra in terms of a multi-component high-velocity outflow in §4. Deconvolution of the kinematic structure of this outflow and detailed modeling of its components is presented in §5. We examine and discuss the implications of our results for the final stages of the transformation of an AGB star into a PN in §6. We present our conclusions in §7.

2. Observations

Using the Fourier Transform Spectrometer at the coudé focus of the Kitt Peak 4-m Mayall telescope, we observed the $4.6 \mu\text{m}$ lines of the fundamental CO vibration-rotation band at 7 different epochs (1988 Nov 30, 1988 Dec 1, 1989 Jan 19, 1989 Nov 3, 1989 Nov 5, 1989 Nov 22, and 1990 Nov 10) in the $2100\text{--}2200 \text{ cm}^{-1}$ range, at an unapodized resolution of 0.02 cm^{-1} ; the spectra were oversampled and recorded at a resolution of 0.0089 cm^{-1} . Data were reduced as described in (Sahai & Wannier 1985). Briefly, each spectrum was divided by the instrumental frequency-response determined by observing a tungsten lamp source. The spectra were then corrected for telluric absorption at the air mass of the source observation as derived from a lunar spectrum divided by the lamp source and an empirically derived 314 K blackbody function for the Moon. We have used $V_{lsr} = -16 \text{ km s}^{-1}$ for the stellar radial velocity, V^* , a value which lies between earlier measurements (-14 to -16 km s^{-1} : Knapp & Morris 1985, Zuckerman & Dyck 1986, KJY97) and more recent ones (-17.5 km s^{-1} : Kahane et al. 1996, Hetal04). The spectra have been normalized to a local continuum level of unity with an uncertainty level of ~ 0.05 . Representative CO ($v = 0 - 1$) spectra (P3, R1, R5, and R7) from each epoch (except 1989 Jan 19, for which the Moon spectrum for telluric correction was not available) are shown in Figure 1.

3. Results

3.1. CO Absorption Features

We first examine the qualitative absorption-line characteristics of the most common CO isotopomers. The signatures (absorption features) of the different outflows (e.g., the normal and HV outflows) are cleanly separated in the $4.6\ \mu\text{m}$ spectra (Fig. 2), unlike the case of mm-wave CO emission spectra taken with telescopes whose beams do not adequately resolve the emitting region. The CO ($v = 0 - 1$) lines show a component extending from roughly $V_{lsr} \approx -15$ to $-43\ \text{km s}^{-1}$ with peak fractional absorption of roughly 50–60%. This is the normal component (hereafter labeled “N”) resulting from absorption in the slowly-expanding CSE around V Hya. The peak absorption in the normal component occurs around $V_{lsr} \sim -28\ \text{km s}^{-1}$, implying an expansion velocity for the slow outflow near $12\ \text{km s}^{-1}$. However, the normal component shows definite structure – shoulders can be seen in each wing of the CO ($v = 0 - 1$) normal component – indicating the presence of kinematic perturbations superimposed on the slow spherical outflow. Of note, the blue wing of the normal component is anomalously wide compared to typical values (few tenths to $1\ \text{km s}^{-1}$) believed to be appropriate for the CSEs of mass-losing AGB stars (see, e.g., Sahai 1990, Teyssier et al. 2006). The half-power point of the normal absorption feature lies roughly $9\ \text{km s}^{-1}$ beyond the velocity of peak absorption, significantly larger as the values observed in other AGB stars (less than a few km s^{-1} : Sahai 1990).

In addition to the normal component, we see prominent absorption in the $V_{lsr} \approx -75$ to $-115\ \text{km s}^{-1}$ region, with a fractional absorption of 5–50%. This absorption arises in gas expanding at much larger velocities than in the slow outflow. The HV absorption feature is complex, with at least six discrete, partially overlapping features, which imply the presence of a corresponding number of distinct kinematic components. These have been labeled H1 through H6, with H1 the bluemost feature (Fig. 2). There is also weaker absorption

extending blueward of $V_{lsr} \approx -115 \text{ km s}^{-1}$, which is best seen in the spectra of the P3, R8, and R7 lines (Fig. 3). Each of these have been chosen as they have no contaminating lines⁴ bluewards of the H1 component, up to $V_{lsr} = -175 \text{ km s}^{-1}$. The HV absorption “tail” extending to about $V_{lsr} = -155 \text{ km s}^{-1}$ is clearly seen in the high signal-to-noise average of the three spectra. Thus we conclude that the HV outflow contains gas expanding at velocities up to 140 km s^{-1} . Weak absorption can also be discerned in the spectral region between the normal and HV outflows ($V_{lsr} = -45$ to -70 km s^{-1}).

In order to be able to select the least contaminated CO lines for analysis, we examine the absorption strengths of $v = 0 - 1$ lines from other isotopomers, as well as the $v = 1 - 2$ lines of CO. In Figure 4, we show averages of 2 to 4 individual lines for each of the possible contaminants. The lines for each contaminant have been selected to include only those which do not have overlapping features from CO or other isotopomers in the normal or HV regions. The strongest two contaminants are CO ($v = 1 - 2$) and ^{13}CO ($v = 0 - 1$).

Within the velocity interval covered by the CO ($v = 0 - 1$) normal component, the CO ($v = 1 - 2$) line shows two local absorption minima, at LSR velocities of -35 km s^{-1} and -14 km s^{-1} . These absorption features occur at the same velocities as the shoulders in the wings of the CO ($v = 0 - 1$) normal component, but are significantly stronger than the absorption due to the normal component of CO ($v = 1 - 2$), and thus provide us a method for measuring their center velocities accurately. This is important, because even though these components are only present weakly in the wings of the CO ($v = 0 - 1$) normal component, they can potentially shift the apparent velocity of the peak of the cool normal component from its actual value. We have therefore first made Gaussians fits to the CO ($v = 1 - 2$) normal absorption features to determine the precise velocity centers of the

⁴i.e., overlapping lines from the $v = 0 - 1$ band of other CO isotopomers, such as ^{13}CO , C^{17}O , or C^{18}O , or the $v = 1 - 2, 2 - 3, \dots$ bands of ^{12}CO and its isotopomers

–35 and –14 km s^{–1} absorption features, and using these centers as fixed inputs, we have made a 3-gaussian fit to the CO ($v = 0 - 1$) normal absorption feature. This yields a peak absorption velocity of $V_{lsr} = -26.3$ km s^{–1} for the main feature, giving an outflow velocity of 10 km s^{–1} for the slow outflow.

¹³CO ($v = 0 - 1$) has a normal absorption component with maximum absorption depth of 20%, and only marginal HV absorption. C¹⁷O ($v = 0 - 1$) has weak normal absorption with a fractional depth of 10% and no obvious HV features. There are no detected features for the C¹⁸O molecule.

Given these restrictions, we chose spectral windows with $\Delta\nu = 2.6$ cm^{–1} ($\Delta V = 360$ km s^{–1}) around individual absorption lines which are free from strong telluric lines or absorption features from contaminants. We have chosen the CO ($v = 1 - 0$) R1, R2, R5, R7, R8, P1 and P3 lines. However, there are small regions of the spectral windows for these lines which are contaminated. The normal components of CO ($v = 1 - 0$) P1 and P3 are contaminated by atmospheric absorption and by CO ($v = 1 - 2$) R3, respectively. The normal feature of CO ($v = 1 - 0$) R7 is overlapped by CO ($v = 1 - 2$) R15. The normal component of CO ($v = 1 - 2$) R13 partially overlaps the H1 component of CO ($v = 1 - 0$) R5, causing it to broaden. The HV region of CO ($v = 1 - 0$) R8 is unusable due to overlapping CO ($v = 1 - 2$) R16 and R24 absorption. Therefore, we have not used the normal absorption features of CO ($v = 1 - 0$) R7, P1, and P3 in the following analyses.

3.2. Time Variations

The high-velocity absorption features were found to change with time in the SW88 study, over the 2 epochs (separated by slightly over 1 year) at which spectra were taken. In order to search for time variations in the outflows in our data, we have calculated the ratios

of absorption intensities, integrated over selected velocity bins, in the CO ($v = 1 - 0$) R1, R2, R5 and R7*⁵ lines for each epoch of observation⁶. We define three velocity bins, labeled N, Hb, and Hr (see Fig. 2). The “N” bin spans the normal component from $V_{lsr} = -10$ to -40 km s^{-1} . Hb and Hr cover the HV region, with Hb spanning the three bluemost features H1, H2, and H3 ($V_{lsr} = -110$ to -94 km s^{-1}) and Hr spanning the three remaining redward components H4, H5, and H6 ($V_{lsr} = -94$ to -76 km s^{-1}). Errors in the integrated intensities have been calculated based on uncertainty in the continuum level and RMS noise. We show the ratios of Hr and Hb to N for each epoch and transition in Figure 5. Dramatic variations can be seen in the ratios from one epoch to the other, including the shortest time scale of two days sampled between 1988 Nov 30 and Dec 1. These variations show that significant changes are occurring in one or both outflows over very short timescales. This timescale limits the size of the region where the changes are occurring to $\lesssim 10^{16} \text{ cm}$, based on the light-crossing time. Thus, the changes most likely arise in the HV outflow, given that the N component is due to absorption in the extended mass-loss envelope of V Hya. It is clear that the changes in the low-J lines (R1, R2) are much more pronounced than in the high-J lines (R5, R7). We have no simple explanation of this effect. We note that infrared pumping due to the $4.6\mu\text{m}$ continuum is expected to affect the population of the low-J levels more than the high-J ones (Schoenberg 1988), so it is possible that fast variations in the $4.6\mu\text{m}$ continuum may play a role in producing this effect: a detailed excitation calculation is required to assess its importance. Numerical simulations of an episodic,

⁵the * denotes our use of the normal absorption component from the R8 line as a proxy for the same in R7, due to the overlap of the CO ($v = 1 - 2$) R15 line in the normal component region of R7

⁶epoch 1989 Jan 19 has been included here because the ratios of the equivalent widths are not affected by the lack of Moon spectra for telluric correction for this epoch

collimated high-velocity outflow interacting with an extended AGB mass-loss envelope are needed to investigate if sufficiently rapid local changes in density and temperature can be produced which may contribute to this effect.

4. The Multi-Component Molecular Outflow in V Hya

Our near-infrared data, together with millimeter-wave and optical spectroscopy, show the presence of multiple molecular outflows in V Hya. As better (high angular resolution, higher sensitivity) millimeter-wave CO data have become available, authors have constructed increasingly detailed models of these outflows on the basis of the line profiles and maps (Kahane et al. 1988, 1996, KJY97, Hetal04). The most recent of these is by Hetal04, which is based on interferometric mapping of the CO J=2-1 emission. This model has 3 kinematic components, defined as a (i) low-velocity, expanding, flattened “disk-like” envelope, with $\Delta V = \pm 8 \text{ km s}^{-1}$ around the systemic velocity, (ii) a medium-velocity wind, with $\Delta V = \pm 60 \text{ km s}^{-1}$, and (iii) a high-velocity jet, with $\Delta V = \pm(60 - 160) \text{ km s}^{-1}$. Hetal04 show that the axis of the high-velocity jet is perpendicular to the major axis of the envelope and the medium-velocity wind. Since Hetal04 only recover $\sim 50\%$ of the single-dish CO J=2-1 flux in their maps, it is clear that they have resolved out a more extended component, which presumably is the slowly expanding, spherical mass-loss CSE. KJY97, from their single-dish spectra of CO J=3-2, CS J=5-4 and HC₃N (25-24) lines, identify such an extended component, expanding at an (uncertain) speed of 15 km s^{-1} , as the “normal” slow AGB wind.

The normal absorption feature arises in the region where the line of sight intersects the slowly-expanding normal CSE (resolved out in the SMA data: Hetal04) and the flattened disk-like envelope. The HV features arise in the region where the line of sight crosses the HV outflows. The absorption occurring at outflow velocities between those of

the normal and HV components could arise in the region where the HV outflows interact with the slow outflow; we therefore call it the “interaction region”. Although the expansion velocity represented by this feature apparently suggests that it is associated with the medium-velocity wind described by Hetal04, such an interpretation is inconsistent with the blue-shift of the “interaction region” features. This is because the medium-velocity wind is red-shifted on the side of the star that shows the blue-shifted HV outflow (and which is responsible for the HV features in our data). The strength of the absorption in the interaction region increases from CO R1 to R8, showing that it arises in highly-excited gas. High excitation temperatures are expected in this region because of deposition of kinetic energy of the HV outflow as it is decelerated by the slow wind.

4.1. High-Velocity Outflow Temperatures

The integrated absorption intensity over the full HV region increases by a factor of 1.6 from CO R1 to R5, and by 1.2 from R5 to R7. Thus the absorption arises in a region of highly-excited gas. Assuming that the absorption is optically thin, we can use the linear part of the curve of growth to calculate the temperatures for each of the three integrated intensity components. The populations in the individual J levels have been calculated using the equivalent width of the corresponding transitions, and plotted against E_J/k . An example of such a plot is shown in Figure 6. If LTE prevails, then all the points should fall on a straight line with a slope equal to $-1/T$ where T is the temperature. Clearly the data cannot be fitted with a straight line, implying that the absorbing column of gas cannot be characterized by a single temperature. Nevertheless, a straight-line fit gives us a rough estimate of the excitation temperatures in the outflow components, yielding $T_{Hb} = 117 \pm 9$ K and $T_{Hr} = 243 \pm 61$ K. Many authors have chosen to fit such plots using two-temperature fits, with one linear fit to the low- J points, and another to the high- J data. However, we

adopt a more sophisticated approach, described below. Such an approach is necessary, not only because a single-temperature fit is incorrect, but more importantly, because the R1 and P1 data points, which represent the population of the $J = 1$ level and should coincide, are significantly separated, implying that these lines are not optically thin, i.e., we cannot assume that $\tau \ll 1$.

5. Detailed Modelling

We now describe a model in which the absorbing column is characterised by a continuous density and temperature distribution. We assume that each of the HV absorption features arises in a shell of gas expanding radially away from the star. Each shell is assumed for computational convenience to have spherical curvature, a constant expansion velocity, an inverse square molecular density dependence on radius, and a power-law excitation temperature characterizing the rotational ladder. We define each shell in terms of 6 parameters: (1) the mass-loss rate \dot{M} , (2) the mean shell radius $\langle r \rangle$, (3) the fractional shell thickness δr (i.e., the outer and inner radii of each shell are $r_{\pm} = \langle r \rangle(1 \pm \delta r/2)$), (4) the excitation temperature $T_{\langle r \rangle}$ at radius $\langle r \rangle$, (5) the power-law exponent for the temperature variation β such that $T(r) = T_{\langle r \rangle}(r/\langle r \rangle)^{-\beta}$, and (6) the intrinsic line width ΔV_t (set by turbulent broadening). The parameters \dot{M} and $\langle r \rangle$ are degenerate, since if each of these is scaled by the same factor, the total absorption column density, N , remains unchanged. Hence we can only determine the ratio $\dot{M}/\langle r \rangle$ from our modelling.

The calculation of the equivalent width of each P- or R-branch line for an adopted set of model parameters is explained in Appendix §A. For each kinematic component modelled, the expansion velocity is fixed at the value determined from Gaussian line-fitting, described in Appendix §B. The relative abundance (by number) of CO to H₂, f_{CO} , is fixed at 4×10^{-4} for all components. Our modelling essentially yields the CO column density for

each component, which is proportional to $\dot{M} f_{CO}$, hence the inferred values of \dot{M} can be easily scaled for a different value of f_{CO} .

5.1. Model Results

We performed model fits for the observed equivalent widths of the CO R1, R2, R5, R7, P1, and P3 transitions for the H1, H2, H3 and H5+ components for each epoch, except 1989 Jan 19, because we did not have associated calibration spectra for the latter. The measurement of these widths from our data is described in Appendix §B. The equivalent width data for the H4 component were not modelled since this component is very weak and has large relative uncertainties. For each component, we found the range of parameters that yield model equivalent widths which are all within $\pm Q\sigma$ of the measured values, where σ is the measured uncertainty in the equivalent width values and Q is a “tolerance” factor. Each fit was performed with a tolerance of $Q = 1.5$, except for the H1 component from 1988 Nov 30, which could only be fit with $Q = 2$. We stepped each parameter’s value in small increments through a large parameter space defined by reasonable minimum and maximum values, which are listed in Table 1. Once the full parameter space was explored, the range of acceptable values was determined as the weighted average of all those which satisfied our fitting criterion as described above, using standard χ^2 weighting.

The best fit values of the 5 model parameters, and the column density N inferred from these for each high-velocity component, are summarized in Table 2. Although the model fitting was carried out for each epoch, the differences in the fitted parameters from epoch to epoch are within the uncertainties of the values derived for each epoch, hence only average values of the parameters are provided.

For the three major kinematic components (H1, H3, H5+) of the HV outflow, the

ratio of the mass-loss to average radius lies in the range 2.4 – 4.4 (in units of $10^{-5} M_{\odot} \text{ yr}^{-1}/10^{16} \text{ cm}$), their column densities are $\sim (1 - 4) \times 10^{17} \text{ cm}^{-2}$, and the fractional shell thickness is about 0.7–0.9 (Table 2). The temperature at the average radius ranges from about 115 to 575 K, and the exponent of the power-law temperature gradient is in the range -1.5 to -2 .

5.1.1. Mass-ejection Rates

We can derive mass-loss rate values for each of the high-velocity kinematic components, if we can constrain the average radius of the shells producing these. SW88 found that the HV features had to be produced in a region with an angular size smaller than $\sim 2.5''$, corresponding to $1.4 \times 10^{16} \text{ cm}$ at a distance of 390 pc (Rowan-Robinson & Harris 1983). If we assume the upper limit for the thickness of the shells based on the time-variations, i.e., 10^{16} cm , then, using our model values of the shell thickness to radius ratio, the typical shell radius is $< 10^{16} \text{ cm}$. Hence the radius of the shells appears to be $< 10^{16} \text{ cm}$, based on two independent arguments. The mass-loss rates of the major components (H1, H3, H5+) thus lie in the range $> (2 - 4) \times 10^{-5} M_{\odot} \text{ yr}^{-1}$.

But note that these values of the mass-loss rate are really proxies for the absorption column density, and do not provide the actual mass-ejection rate per year, \dot{M}_{HV} , for the material observed in the HV $4.6 \mu\text{m}$ absorption features. The latter can only be calculated by scaling our model values by the solid angle, ω (as a fraction of 4π) subtended by the absorbing material at the star – our data do not provide this information. However, given the highly collimated nature of the HV outflow, it is likely that ω is significantly smaller than unity. We can make a rough estimate of ω by noting that the values of the (projected) opening angle measured for the optical outflow (20° – 30° , Setal03), and that (24°) derived from the size of the most distant, high-velocity blue-shifted CO J=2-1 blob ($5''$ at a radius

of about $12.5''$; Hetal04), are very similar. Hence, we use a deprojected opening angle of $25^\circ \text{Sin}i$ (where i is inclination angle of the fast outflow to the line of sight) for the shells producing the HV $4.6 \mu\text{m}$ absorption features. We find that $\omega = 1.2 \times 10^{-3} \text{Sin}i$; taking $i=25^\circ$ (mean of the values suggested by Setal03 and Hetal04), we obtain $\omega = 5.2 \times 10^{-4}$, and the mass-loss rates for the major HV components, $\dot{M}_{HV} > (1 - 2) \times 10^{-8} M_\odot \text{yr}^{-1}$.

In comparison, the mass-loss rate for the HV outflow estimated from the single-dish CO J=3-2 and 2-1 data (KJY97) is larger by more than 2 orders of magnitude. They compute this rate by deriving the total mass of the high-velocity outflow from the CO fluxes using a constant density LVG code, and then dividing this by an expansion time-scale derived from the outer radius, assumed to be 5×10^{16} cm, a value supported by the CO J=2-1 position-velocity maps by Hetal04 which show the high-velocity outflow extending to about $10''$ - $12.5''$, or $(5.7 - 7.3) \times 10^{16}$ cm on either side of the center. KJY97 find, for the high-velocity outflow, $\dot{M} = 7.4 \times 10^{-6} M_\odot \text{yr}^{-1}$, or $1.85 \times 10^{-5} M_\odot \text{yr}^{-1}$ after scaling to our lower value of the fractional CO-to-H₂ abundance ratio. The discrepancy between the HV mass-loss rates as derived from the mm-wave lines and the $4.6 \mu\text{m}$ lines implies that only a small fraction of the total HV gas in V Hya is at the high temperatures we derive (i.e., > 100 K).

5.1.2. Kinetic Temperatures

The kinetic temperature in the outflows is extremely sensitive to the ratio of the absorption intensities of high- J to low- J transitions. We note that the H₂ component is produced in markedly cooler gas, compared to the other three components. We find that, with the exception of the H₂ component, the outflow temperature increases with decreasing expansion velocity of the outflow. A plausible explanation for this trend is, assuming the outflows are gas parcels (“bullets”) which are ejected with the same velocity from the

center, that the slower components are those which have interacted more extensively with the ambient circumstellar material, and thus have had a larger fraction of their kinetic energy converted into thermal energy. The derived temperature dependence $r^{-1.5 \pm 1.0}$ shows that there is a significant radial temperature gradient in each component, as one may expect in regions of strongly-shocked gas (e.g., Lee & Sahai 2003).

5.1.3. Line-Widths

In our model fitting, we have allowed the intrinsic line width, ΔV_t , to act as a free parameter. We can thus compare the model values of ΔV_t to the observed FWHM values of the absorption features as an independent test of our modeling. We find that the model line width values (6.4, 2.4 and 6.5 km s⁻¹ for H1, H2, H3; Table 2) agree reasonably well (i.e., within 3σ) with those derived from fitting the line profiles (7.9 ± 1.2 , 3.8 ± 0.8 and 8.8 ± 1.8 km s⁻¹ for H1, H2, H3), taking into account the intrinsic resolution of the spectra, which is about 2.8 km s⁻¹. For the H5+ component, which is a combination of H5 and H6, the model ΔV_t is 9.1 km s⁻¹. In comparison, H5 and H6 have ΔV_t values of 7.5 ± 3 and 7.9 ± 1.8 km s⁻¹, which combined together, give 10.9 ± 3.5 km s⁻¹.

Thus both our observed and model values of the intrinsic line widths are quite large compared to the typical values ($\sim 1 - 2$ km s⁻¹) used for modelling normal AGB CSEs. Low values of ΔV_t result in the model lines becoming very optically thick, making their equivalent widths relatively insensitive to changes in column density or temperature. In this very optically thick regime, a good fit to the data, which show that the low- J lines have significantly smaller equivalent widths than the high- J lines, is not possible. Reasonable fits are obtained only when $\Delta V_t \gtrsim 5$ km s⁻¹ (except for H2).

The presence of large turbulent velocities is physically intuitive, since the energetic

hydrodynamic interaction of the HV gas with the slowly expanding dense outflow will produce shock-waves and instabilities which increase the turbulence in both the HV and the normal outflow. But there is a caveat to this explanation of the large line-widths – there may be a significant contribution to the latter due to systematic velocity gradients in the absorbing columns for each component. However, both large intrinsic line-widths and large velocity gradients have the same qualitative effect on (i.e., a reduction in) the optical depth at any particular velocity, so we do not expect that our model results will be affected very significantly were we to include a velocity gradient in our model.

5.1.4. *Absorption Feature Overlaps*

The different absorption features extracted using our Gaussian fitting overlap in their wings. These overlaps will result in radiative interaction between the shells producing the absorption for each of these features. Our model fits the resulting equivalent widths of each of these features independently, implicitly ignoring this radiative interaction – such a procedure is acceptable if the optical depths are small, but if they are $\gtrsim 1$, then the uncertainties in the derived results could be significant. However, radiative interaction between the different components is not a significant source of uncertainty for our modelling results because (i) the intrinsic peak optical depth of each component is modest, and (ii) the overlap occurs at velocities close to or beyond the half-power point for each Gaussian component, where the optical depths are significantly lower than those at the peak. For example, for the deepest absorption features (R7, H6 and R5, H3), the average (over epochs) ratio of the intensity at the center of the line to the continuum is about 0.6, hence the largest peak optical depth is about 0.5. The velocity ranges (relative to the systemic velocity) spanned by the three strongest components H1, H3, and H5+ over their measured widths (FWHM values, corrected for the instrumental resolution), respectively are -95 to

–87.9, –85.7 to –77.4, and –73.0 to –62.5 km s^{–1}, hence the overlaps of these components occur beyond their half-power range. Since the Gaussian function representing each component falls rapidly beyond its half-power point, the optical depth of each component in the overlapping velocity range is quite small. Only the H2 component, which spans the velocity range from –87.0 to –84.4 km s^{–1}, has a closer overlap than the others with its neighbouring component, H3. However, since the H2 component is optically thin (with optical depths $\lesssim 0.15$), it is unlikely to affect the H3 component.

The inferred fractional widths of the shells for the H1, H3 and H5+ components are only modestly less than unity (δr in Table 2), i.e., the shells are geometrically thick. Our modelling does not determine the actual average radius for each of the shells, but in order to avoid spatial overlaps between these, their average radii must be spread over at least a factor of about 5.5. For example, a possible shell configuration which avoids spatial overlaps and satisfies the criterion that $\langle r \rangle < 10^{16}$ cm (see § 5.1.1), has $\langle r \rangle = 1.8 \times 10^{15}$, 4.4×10^{15} and 9.9×10^{15} cm for the H5+, H3, and H1 components⁷. We note however, that since δr depends on the exponent of the model density power-law, $\rho(r) \propto r^{-p}$ ($p = 2$ in our modelling), and steeper exponents will result in smaller values of δr , the required spread of average radii could be less than 5.5, if $p > 2$.

6. Discussion

V Hya is believed to be at a short-lived but critical stage in the evolution of a mass-losing AGB star into a bipolar PN (Tsuji et al. 1988; Kahane et al. 1996), and has been dubbed a “nascent” PPN (Sahai 2007). Based on their imaging survey of young

⁷We have chosen a physically plausible configuration in which the average shell temperature, $T_{\langle r \rangle}$, decreases with radius, but this is not required

PNs, Sahai & Trauger (1998) proposed that collimated fast winds (CFWs) are the primary mechanism for the dramatic change in circumstellar geometry and kinematics as stars evolve off the AGB. Such jets have been invoked by Soker (1990) to explain the presence of ansae in PNs. Sahai et al. (2007) carried out a survey of pre-planetary nebulae, and found strong similarities in morphologies between PPNs and young PNs, supporting Sahai & Trauger’s hypothesis that the CFW’s begin operating during the PPN phase or even earlier, during the late AGB phase. V Hya provides the best and most detailed example of a (carbon-rich) AGB star in which the CFW’s, which are hypothesized to begin the shaping process, are so clearly manifest.

The near-infrared observations presented here probe the CFW on intermediate scales (~ 1000 AU), beyond the very small scales probed by the optical data of Setal03 ($< 0.4''$ or 150 AU). The interferometric mm-wave CO data mostly probes larger scales, between a few arcseconds to $\sim 15''$. These three datasets clearly attest to the episodic nature of the V Hydrae HV outflow. Blobby emission is seen in both the CO interferometric maps of the HV outflow (panels *a,c* of Fig. 2 in Hetal04), and the optical HV emission (Fig. 1 of Setal03). The multiple kinematic components which we find from our $4.6\mu\text{m}$ data directly show that the HV outflow is discontinuous in velocity space, and, as our modelling results indicate, the absorbing matter is organised (at least radially) into discrete spatial structures. We conclude that the HV outflow in V Hya has consisted of discrete blobs (i.e., bullets) throughout its observed history ($\sim 100\text{-}250$ yr). These bullet-like ejections are actively sculpting the mass-loss envelope of V Hya from the “inside-out”, into a bipolar PPN. V Hya is not alone amongst AGB and post-AGB objects in which high-velocity outflows appear to be organised in knots/bullets: other prominent examples are the PPNs, Hen 3-1475 (e.g., Velázquez et al. 2004) and IRAS 22036+5306 (Sahai et al. 2003b), and the PNs, Hen 2-90 (Sahai et al. 2000) and MyCn18 (O’Connor et al. 2000).

V Hya is thus a key object in helping us understand how aspherical planetary nebulae are formed, and should be the focus of new observational and theoretical efforts. For example, a renewed effort using STIS to follow the evolution of the optically-detected high-velocity outflow should be made, assuming that the upcoming Hubble servicing mission repairs STIS⁸. Near-infrared interferometry at milliarcsec resolution (i.e., few AU at V Hya’s distance) using the VLTI AMBER instrument should be used to probe the central engine which is producing the high-velocity bullets. 3-D hydrodynamic numerical simulations of such bullet-like outflows interacting with an AGB mass-loss envelope (e.g., Dennis et al. 2008) should be carried out to see if they can reproduce the salient observational features of the high-velocity outflows in V Hya.

7. Conclusions

We have obtained high-resolution spectroscopic data at $4.6\mu\text{m}$ of the carbon star V Hya, using the Fourier Transform Spectrometer at the coudé focus of the Kitt Peak 4-m Mayall telescope. These data, taken over 7 epochs spanning 2 years, cover a large number of P– and R– branch transitions in the fundamental vibration-rotation band of CO and its isotopomers. We find:

(i) The circumstellar environment of V Hya consists of a slow-moving normal outflow at about 10 km s^{-1} , and a complex high-velocity outflow containing at least six kinematic components with expansion velocities ranging between 70 and 120 km s^{-1} . Weaker absorption can be seen extending to blue-shifted velocities upto 140 km s^{-1} .

(ii) Physical changes occur in the high-velocity outflow regions on a time-scale as short as two days, which constrains their extent to be $< 10^{16}\text{ cm}$.

⁸such a program spanning 3 years was unfortunately cut short due to STIS’s demise

(iii) The absorption in the high-velocity features is not optically thin, i.e., we cannot assume that $\tau \ll 1$. The strongest features have typical optical depths of about 0.5. Using a non-linear, multi-parameter best-fit model, we can characterize each of the kinematic components in terms of its measured expansion velocity, the ratio of the mass-loss rate to the average shell radius (a proxy for the absorption column density), the fractional shell thickness, a temperature power-law, and an intrinsic line width.

For the three-most intense kinematic components, the column density is $\sim (1 - 4) \times 10^{17}$ cm^{-2} ; the fractional shell thickness is about 0.7–0.9; the temperature at the average radius ranges from about 115 to 575 K, and the exponent of the power-law temperature gradient is in the range -1.5 to -2 .

(v) The (projected) opening angle of the outflow (25°), does not vary significantly from small ($0.25''$) to large radii ($12.5''$), as sampled by the optical and millimeter-wave observations. Assuming the same value for the high-velocity outflow seen in the $4.6\mu\text{m}$ data (and an inclination angle to the line of sight of 25°), we find that the mass-ejection rate of material seen in the major HV outflow components lies in the range $\gtrsim (1 - 2) \times 10^{-8} M_\odot \text{ yr}^{-1}$.

(iv) Both the observed and model values of the intrinsic line-widths are quite large ($6 - 8 \text{ km s}^{-1}$ in all except one kinematic component) compared to the typical values ($\sim 1 \text{ km s}^{-1}$) appropriate for the circumstellar envelopes of normal AGB stars. The large widths are probably due to turbulence broadening, and/or systematic velocity gradients, resulting from the energetic hydrodynamic interaction of the high-velocity gas with the slowly expanding dense outflow.

We thank an anonymous referee for helpful comments. RS's contribution to the research described in this publication was carried out at the Jet Propulsion Laboratory,

California Institute of Technology, under a contract with NASA. RS thanks NASA for financial support via *HST* awards GO-9632.01 and GO-9800.01 administered by STScI, and an LTSA award. BEKS acknowledges support from the Department of Physics at Occidental College and the Caltech SURF program.

A. Calculating the Model Equivalent Widths

We compute the absorption intensity for each component in a particular transition ($v = 0, J$) \rightarrow ($v = 1, J'$) at a given velocity as follows. The absorbing shell is divided into a large number of very thin radial zones. The attenuation of incident radiation by each of these thin shells (at a given velocity) can be written as $\exp[-\Delta\tau(r_i, V)]$, where $\Delta\tau(r_i, V)$ is the radial optical depth due to the i^{th} thin radial zone. The optical depth is proportional to the column density, the J -level population in the vibrational ground state ($v = 0$), the infrared matrix element for dipole transitions, and the Gaussian velocity function.

The column density N of CO in the i^{th} thin radial zone is given by:

$$N_i = \left(\frac{1}{r_{i,-}} - \frac{1}{r_{i,+}} \right) \frac{\dot{M} f_{CO}}{4 \pi V_{exp}}, \quad (\text{A1})$$

where $r_{i,\pm}$ are the outer and inner limits of the i^{th} thin radial zone and f_{CO} is the number abundance ratio of CO to H_2 . The populations of the different J levels in the ground vibrational state is found, assuming LTE, using the partition function

$$n_J = \frac{g_J \exp(-E_J/kT)}{Z} \quad (\text{A2})$$

where $g_J = 2J + 1$ is the statistical weight, and

$$Z = \sum_{J=0}^{\infty} g_J \exp(-E_J/kT). \quad (\text{A3})$$

The velocity dependence is described by the Gaussian velocity function

$$\phi(V) = C \exp \left[-4 \ln 2 \left(\frac{\Delta V}{\Delta V_t} \right)^2 \right] \quad (\text{A4})$$

with $\Delta V = V - V_0$, where V_0 is the line center velocity and C is the normalization constant equal to $(\sqrt{4 \ln 2 / \pi}) / \Delta V_t$, and ΔV_t is the intrinsic line width.

The fractional absorption intensity at a given velocity is simply the product of the attenuation factors due to each thin radial zone

$$f(V) = \prod_{i=1}^N \exp[-\Delta\tau(r_i, V)] \quad (\text{A5})$$

The equivalent width is then given by

$$W_\nu = \frac{\nu}{c} \int [1 - f(V)] dV \quad (\text{A6})$$

where the integration range is chosen to be sufficiently large that $1 - f(V) \approx 0$ near the boundaries of this range.

B. Measuring the Observed Equivalent Widths

We calculate the equivalent width of each absorption component by fitting Gaussians to each of the six HV absorption features. The spectra were first smoothed using a three-point (Hanning) filter that averages 50% of each channel with 25% of the adjacent lower and higher channels. Our data reduction package included a non-linear, least squares Levenberg-Marquardt algorithm which allowed the deconvolution of up to three Gaussians at a time. Assuming that there are no HV components blueward of H1, we make a simultaneous 3-Gaussian fit to the triplet consisting of H1 and its two redward neighbors, H2 and H3. The fits for H1 and H2 were then subtracted, leaving H3. In this way we account for Gaussian superposition on the blue side of H3. We then repeat the above

process for the H3–H5 triplet, and finally fit the H5–H6 components. A particular fit to all six components is considered acceptable if minor perturbations in the input parameters yield the same output fit parameters. For all epochs, the residual spectral artifacts following subtraction of all Gaussians were less than 3.5% of the continuum level. Uncertainties in the equivalent widths were estimated by allowing the continuum level to vary by 3.5%, and propagating the effect of this variation on the peak and FWHM of each fitted component.

In some cases, the deconvolution process was not as straightforward as just described, because the absorption-line features are too closely spaced for a unique deconvolution. To address this issue, we assume that the line centers and FWHMs (in velocity space) of such features will not vary significantly over different J transitions. For example, since the R5 and R7 features of the H2 components could be properly separated, we fixed the centers and FWHM of their Gaussians to be the same as the lower- J transitions. Similarly, the lines in the P1 and P3 transitions of the H4 component could not be uniquely deconvolved, hence their centers and FWHM were fixed to be those of the corresponding R-transitions.

The velocity separation between the H5 and H6 components is not always large enough to uniquely deconvolve these components. Therefore, although we fitted Gaussians to each component, we used the sum of the derived areas under the fitted line profiles to equivalent width, labeled “H5+”, for model fitting. The expansion velocity of H5+ is taken to be the average of the velocities of H5 and H6 and the FWHM is the square root of the sum of the squares of the individual FWHM.

REFERENCES

- Balick, B., & Frank, A. 2002, *ARA&A*, 40, 439
- Barnbaum, C., Morris, M., & Kahane, C. 1995, *ApJ*, 450, 862
- Dennis, T. J., Cunningham, A. J., Frank, A., Balick, B., Blackman, E. G., & Mitran, S.
2008, *ApJ*, 679, 1327
- Evans, T. L. 1991, *MNRAS*, 248, 47
- Hirano, N., et al. 2004, *ApJ*, 616, L43
- Kahane, C., Maizels, C., & Jura, M. 1988, *ApJ*, 328, L25
- Kahane, C., Audinos, P., Barnbaum, C., & Morris, M. 1996, *A&A*, 314, 871
- Knapp, G. R., Jorissen, A., & Young, K. 1997, *A&A*, 326, 318
- Knapp, G. R., & Morris, M. 1985, *ApJ*, 292, 640
- Lee, C.-F., & Sahai, R. 2003, *ApJ*, 586, 319
- Luttermoser, D. G., & Brown, A. 1992, *ApJ*, 384, 634
- Morris, M. 1987, *PASP*, 99, 1115
- O'Connor, J. A., Redman, M. P., Holloway, A. J., Bryce, M., López, J. A., & Meaburn, J.
2000, *ApJ*, 531, 336
- Rowan-Robinson, M., & Harris, S. 1983, *MNRAS*, 202, 797
- Sahai, R. 1990, *ApJ*, 362, 652
- Sahai, R., & Wannier, P. G. 1985, *ApJ*, 299, 424

- Sahai, R., & Wannier, P. G. 1988, *A&A*, 201, L9 (SW88)
- Sahai, R., & Trauger, J. T. 1998, *AJ*, 116, 1357
- Sahai, R., & Nyman, L.-Å. 2000, *ApJ*, 538, L145
- Sahai, R., Morris, M., Knapp, G. R., Young, K., & Barnbaum, C. 2003, *Nature*, 426, 261
- Sahai, R., Zijlstra, A., Sánchez Contreras, C., & Morris, M. 2003, *ApJ*, 586, L81
- Sahai, R., Morris, M., Sánchez Contreras, C., & Claussen, M. 2007, *AJ*, 134, 2200
- Sahai, R., Findeisen, K., de Paz, A. G., & Sánchez Contreras, C. 2008, *ApJ*, 689, 1274
- Schoenberg, K. 1988, *A&A*, 195, 198
- Soker, N. 1990, *AJ*, 99, 1869
- Teyssier, D., Hernandez, R., Bujarrabal, V., Yoshida, H., & Phillips, T. G. 2006, *A&A*, 450, 167
- Tsuji, T., Unno, W., Kaifu, N., Izumiura, H., Ukita, N., Cho, S., & Koyama, K. 1988, *ApJ*, 327, L23
- Velázquez, P. F., Riera, A., & Raga, A. C. 2004, *A&A*, 419, 991
- Zuckerman, B., & Dyck, H. M. 1986, *ApJ*, 311, 345

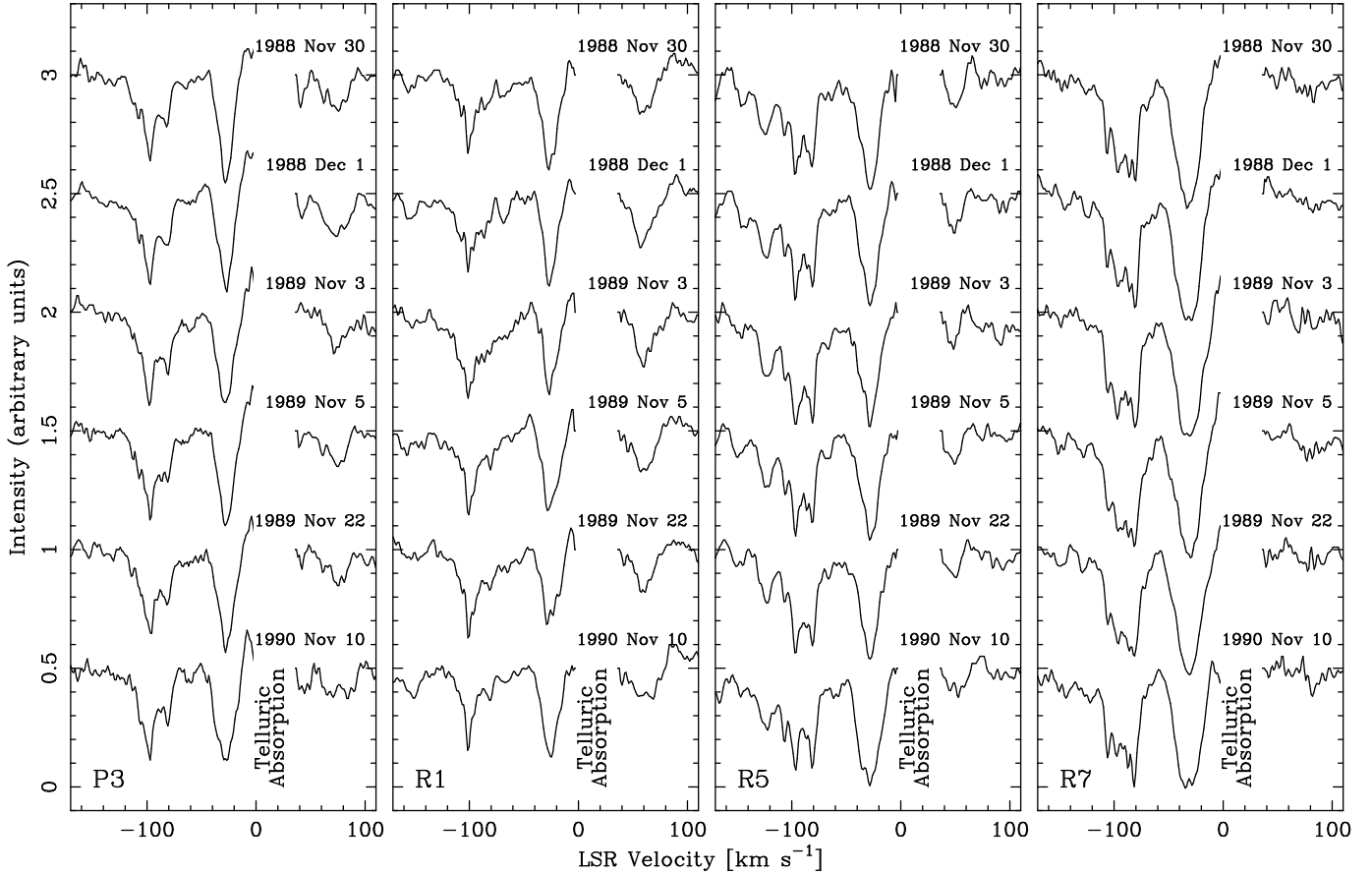


Fig. 1.— Sample spectra of different CO ($v = 1 - 0$) lines (P3, R1, R5, R7) and different epochs. Regions of strong telluric absorption have been blanked out. The continuum levels for the spectra have been scaled to unity, but constant offsets have then been added to them, in order to shift them vertically for clarity in this plot. These offsets are (from bottom to top) -0.5, 0, 0.5, 1.0, 1.5, & 2.0.

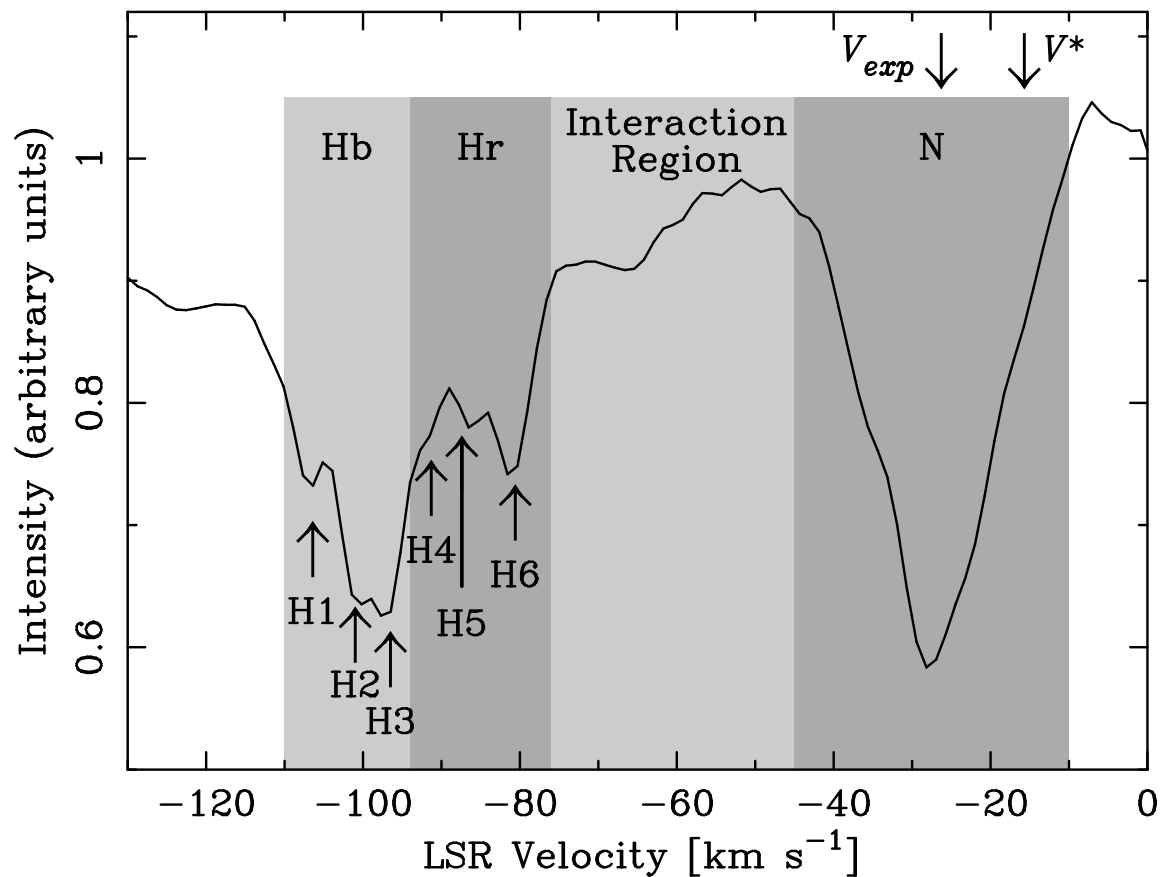


Fig. 2.— Sample CO spectrum produced by averaging the R1, R2, and R5 spectra over all epochs, showing the various velocity regions and individual high-velocity components H1–H6. The continuum level for each spectra was scaled to unity before averaging. Shading denotes broader velocity regions discussed in the text (e.g. §3). The LSR velocities of V Hya and the peak absorption of the normal component (“N”) are marked by V^* and V_{exp} , respectively.

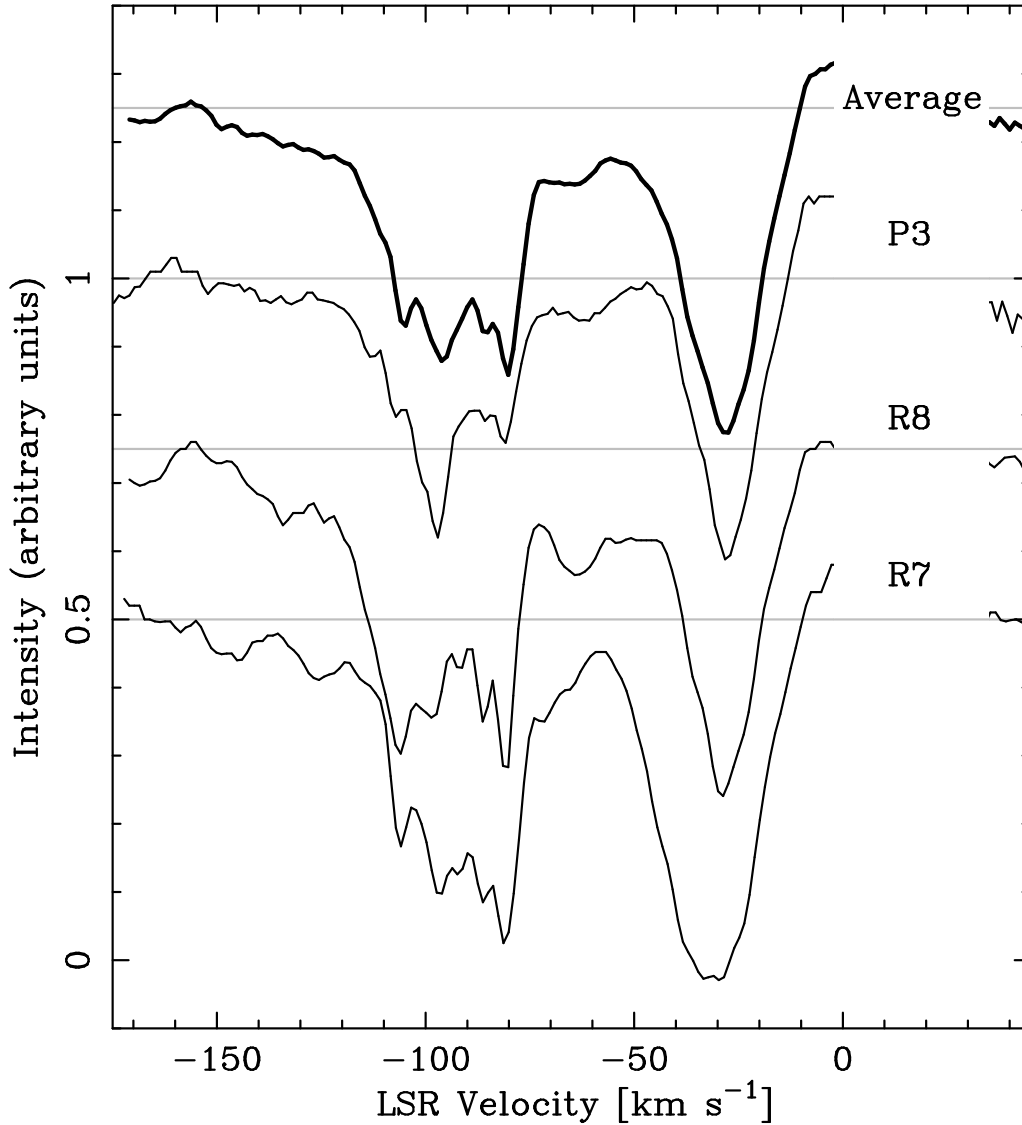


Fig. 3.— CO P3, R7, and R8 spectra averaged over all epochs, plus the average of these spectra, showing the highest-velocity features extending blueward from H1 ($V_{lsr} \approx -110$ km s $^{-1}$) to about -155 km s $^{-1}$. The continuum levels for the spectra have been scaled to unity, but constant offsets have then been added, in order to shift them vertically for clarity in this plot. These offsets are -0.5 (R7), -0.25 (R8), 0 (P3), & 0.25 (Average).

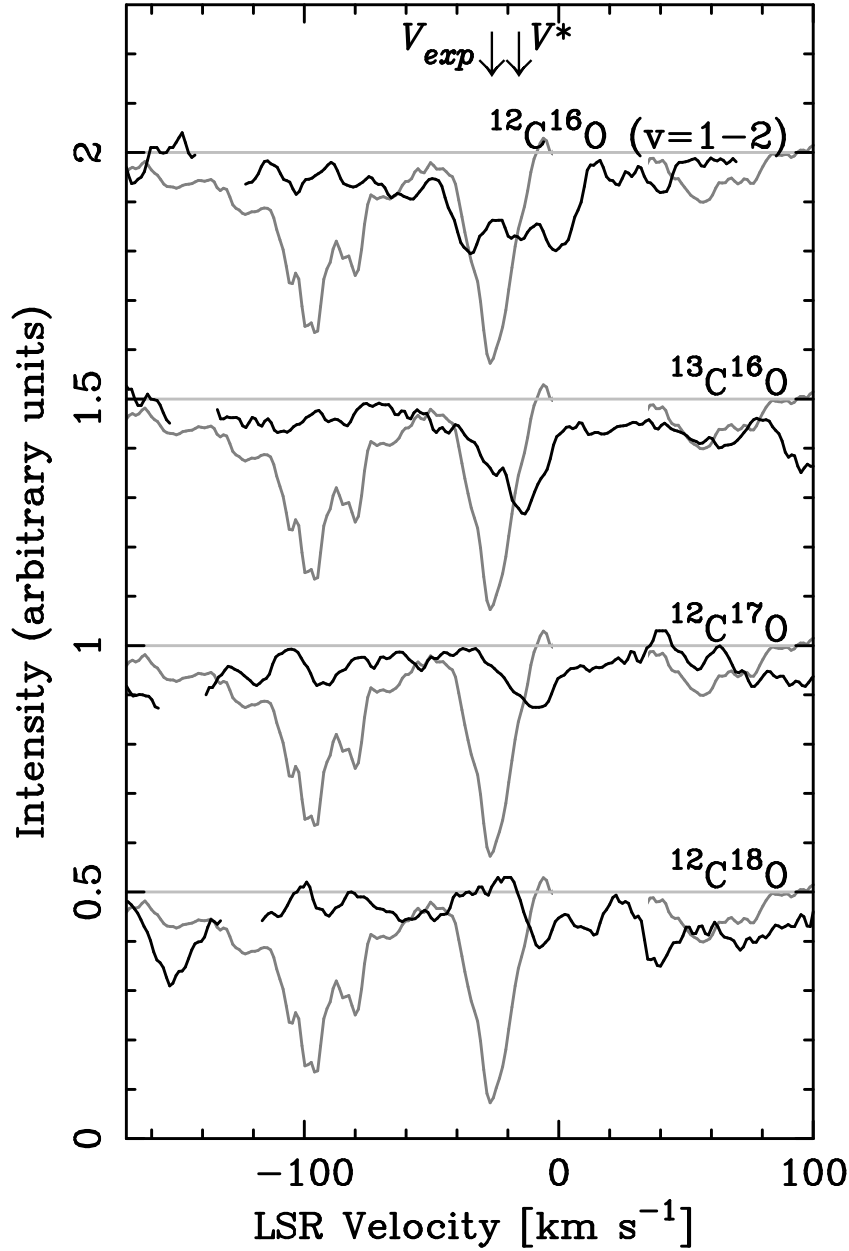


Fig. 4.— Average spectra showing the absorption features of CO ($v = 1 - 2$), ^{13}CO , C^{17}O , and C^{18}O , as marked in each panel, plotted over the average CO ($v = 1 - 0$) spectrum (in grey, from Fig. 2). Regions of strong telluric absorption have been blanked out. LSR velocities of V Hya and the peak absorption of the normal component are marked (as in Fig. 2). The continuum levels (in light grey) for the spectra have been scaled to unity, but constant offsets have then been added, in order to shift them vertically for clarity in this plot. These offsets are (from bottom to top) -0.5, 0, 0.5, & 1.0.

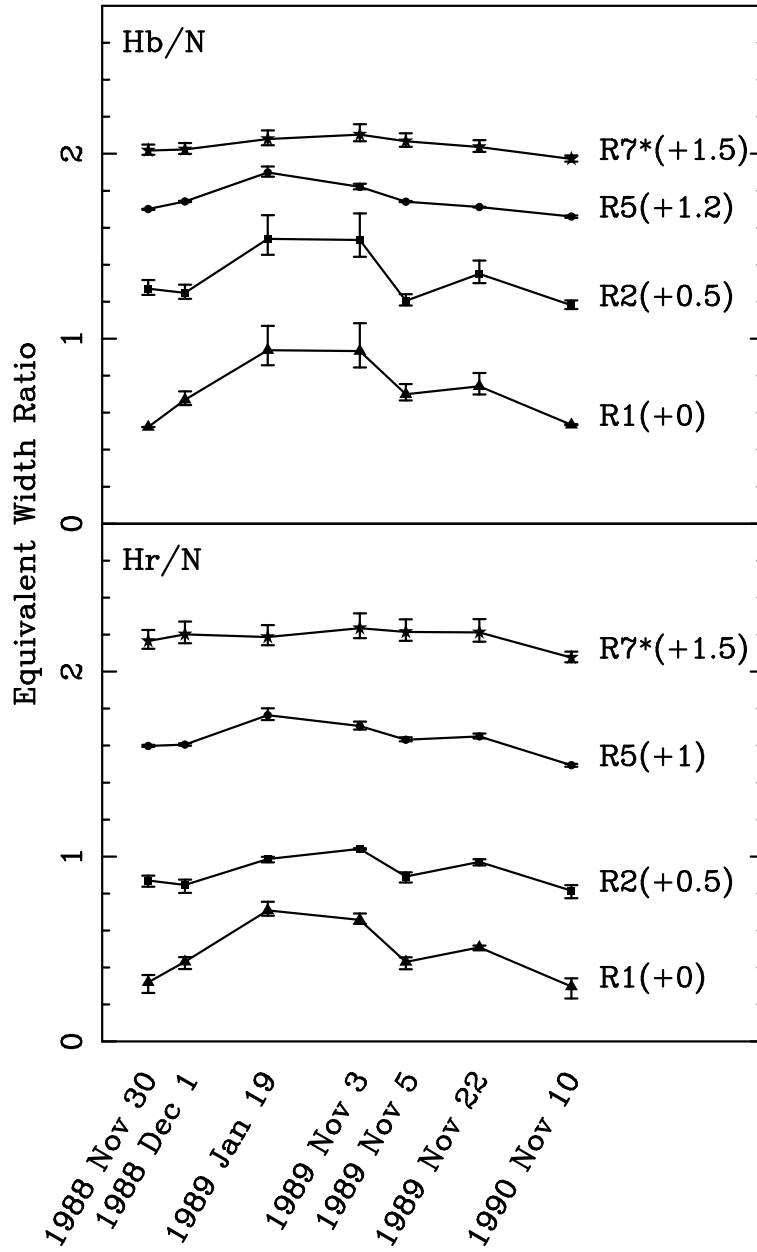


Fig. 5.— Equivalent width ratios of the high-velocity blue (Hb) and red (Hr) components (as defined in the text and Fig. 2) to that of the normal component. Constant offsets have then been added to each of these (as shown) in this plot, in order to shift them vertically for clarity. Epochs are denoted at bottom, and the rotational transitions at right.

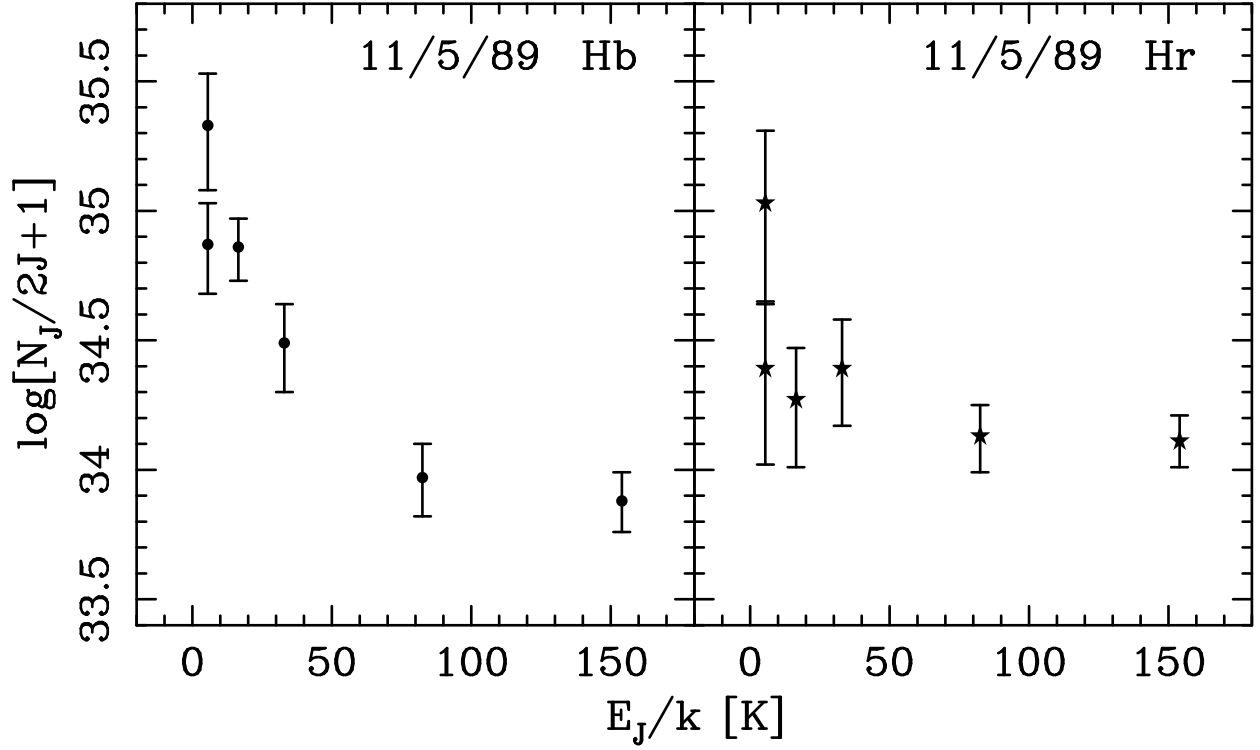


Fig. 6.— Populations of individual J levels, calculated using the equivalent width of the corresponding transitions for the Hb and Hr components, plotted against E_J/k . Note that the R1 and P1 data points ($E_J/k = 5.5$), which represent the population of the $J = 1$ level and should coincide, are significantly separated.

Table 1. Parameter Ranges for Equivalent Width Modeling

Limit	$\dot{M}/\langle r \rangle$	δr	$T_{\langle r \rangle}$	β	ΔV_t
	$10^{-5} M_{\odot} \text{ yr}^{-1}/10^{16} \text{ cm}$		K		km s^{-1}
Minimum	0.005	5×10^{-4}	1	0	1
Maximum	4000	1	1000	10	10

Table 2. Model Fitting Results

Parameter	H1	H2	H3	H5+
V_{exp}^a	91.4	85.8	81.5	67.8
$\dot{M}/\langle r \rangle$	2.4 ± 0.5	0.74 ± 0.16	4.4 ± 0.7	3.3 ± 0.6
δr	0.72 ± 0.12	0.25 ± 0.05	0.90 ± 0.14	0.72 ± 0.12
$T_{\langle r \rangle}$	116 ± 20	32 ± 19	263 ± 28	574 ± 38
β	1.8 ± 0.4	1.5 ± 0.4	1.5 ± 0.4	1.4 ± 0.4
ΔV_t	6.4 ± 0.7	2.4 ± 0.5	6.5 ± 0.6	9.1 ± 0.7
N	0.9 ± 0.3	0.1 ± 0.02	3.7 ± 0.6	2.3 ± 0.2

^a V_{exp} for each component is determined by Gaussian profile fitting as described in § Appendix B

Note. — Units are: V_{exp} : km s^{-1} , $\dot{M}/\langle r \rangle$: $10^{-5} M_{\odot} \text{ yr}^{-1}/10^{16} \text{ cm}$, $T_{\langle r \rangle}$: K, ΔV_t : km s^{-1} , N : 10^{17} cm^{-2} , δr : dimensionless